

Adsorption of a superoxo O_2^- species on the pure and Ca-doped $Sr_3Ru_2O_7(001)$ surface

Wernfried Mayr-Schmölzer^{a,b}, Florian Mittendorfer^{a,b,*}, Josef Redinger^{a,b}

^a*Institute of Applied Physics, Vienna University of Technology, Wiedner Hauptstr. 8-10, 1040 Vienna, Austria*

^b*Center for Computational Materials Science, Vienna University of Technology, Wiedner Hauptstr. 8-10, 1040 Vienna, Austria*

Abstract

Only recently, the activation of oxygen molecules on clean defect-free transition metal oxide surfaces has been reported, for example on the CaO-terminated surface of the Ruddelsden-Popper perovskite $Ca_3Ru_2O_7(001)$. In this work we show that oxygen molecules adsorb as an activated superoxo species on a clean SrO-terminated surface of $Sr_3Ru_2O_7(001)$. At all coverages, the electrons activating the molecule originate from the subsurface RuO_2 layer. At low coverages, the presence of a Ca dopant in the terminating SrO layer slightly increases the adsorption energy. At high coverage, DFT predicts a flat potential energy surface and a preferred adsorption of the O_2^- near surface cations. Advanced many-electron calculations (RPA) predict adsorption energies of -0.99 eV and -0.49 eV per O_2^- molecule for low and high coverages, respectively, and a preference for forming line-like structures in the latter case.

Keywords: Strontium ruthenate, $Sr_3Ru_2O_7$, oxygen, superoxo, O_2^- minus, DFT, GW, RPA

1. Introduction

In recent years, the chemistry of ternary transition metal oxides has garnered increased interest due to their vast potential for applications, ranging from fuel cells to electrocatalysis. In addition, the electronic, magnetic and chemical properties of perovskites of the Ruddelsden-Popper series are often tuneable by doping, applying electric or magnetic fields, or mechanical stress.

Much research has been done regarding the oxygen transport and reduction properties on various perovskite materials [1–4], but the activation of molecular oxygen is less well understood. In particular, the ability to dissociation oxygen molecules plays a key role in current and future applications like solid oxide fuel cells (SOFC). Recently, theoretical and experimental studies have shown that the pristine SrO terminated surface of $SrTiO_3$ does not dissociate adsorbed O_2 molecules. Only in the presence of vacancies the surface

*Corresponding author

activity is increased and adsorption of a charged superoxo O_2^- species was predicted [5]. The defect-free LaO-terminated (001) surface of another Ruddelsden-Popper perovskite, La_2NiO_4 , already shows activation of the O_2 molecule for the stoichiometric surface, as charge is transferred from the surface La atoms to the adsorbed oxygen [6]. Recently, a combined theoretical and experimental study of the (001) surface of $Ca_3Ru_2O_7$ also predicts the adsorption of oxygen as a superoxo species, but in that case a different charge transfer mechanism was identified. In contrast to La_2NiO_4 , charge is not transferred from the A-site cation, but from the conduction electrons close to the Fermi level [7].

In the present paper, we present a theoretical study of the adsorption of O_2 molecules on the (001) surface of pure and Ca-doped $Sr_3Ru_2O_7$. $Sr_3Ru_2O_7$, a Ruddelsden-Popper perovskite structurally closely related to the aforementioned $Ca_3Ru_2O_7$, shows the same SrO surface termination after cleaving as the related binary SrO, but at a larger lattice constant [8].

2. Computational Methods

All calculations were performed with the Vienna *Ab-Initio* Simulation Package (VASP) using the projector-augmented plane wave method [9]. The electronic interactions were described within the framework of Density Functional Theory (DFT) using the spin-polarized van-der-Waals corrected optB86b [10, 11] exchange-correlation functional. For the slab calculations, dense Γ -centered Monkhorst-Pack grids of $6 \times 6 \times 1$ \vec{k} -points were used to sample the Brillouin zone and the energy cutoff for the plane waves was set to 400 eV. Hybrid functional calculations were performed using the HSE06 functional [12]. The RPA total energy calculations are based on the Adiabatic Connection Fluctuation-Dissipation Theory (ACFDT) and were performed for the optB86b-optimized structures using a modern, low-scaling algorithm [13], starting from initial PBE orbitals. All calculations did not take zero point effect into account.

The surface structure was modeled using double-layer slabs of $Sr_3Ru_2O_7$, separated by 24 Å of vacuum. For the low coverage case a $c(4 \times 4)$ unit cell was used, yielding a minimum coverage of 1/16 after adsorption of a single O_2 molecule. The high coverage case was studied by a $c(2 \times 2)$ unit cell with up to four adsorbed O_2 molecules. The \vec{k} -point grids were adjusted according to the size of the reciprocal cell: for the low coverage $c(4 \times 4)$ cell a $3 \times 3 \times 1$ and for the smaller $c(2 \times 2)$ cell a $6 \times 6 \times 1$ Γ -centered \vec{k} -point grid was used, respectively. Due to the computational cost involved in the hybrid (HSE06) and many-electron approaches (G_0W_0 /RPA) only simulations of the $c(2 \times 2)$ model with a reduced $4 \times 4 \times 1$ (HSE06) and $3 \times 3 \times 1$ (RPA) Γ -centered \vec{k} -point grid, were viable.

3. Results

3.1. Pristine Surface

The $Sr_3Ru_2O_7$ crystal is the $n = 2$ member of the Ruddelsden-Popper series $Sr_{n+1}Ru_nO_{3n+1}$. It consists of two perovskite $SrRuO_3$ layers separated by a rock-salt like SrO terminated interface, as shown in Fig. 1. The RuO_6 octahedra are rotated by 6.8° around the [001] direction [14], but in contrast to $Ca_3Ru_2O_7$, no tilting is observed. The connected octahedra within each double row are rotated against each other, resulting in

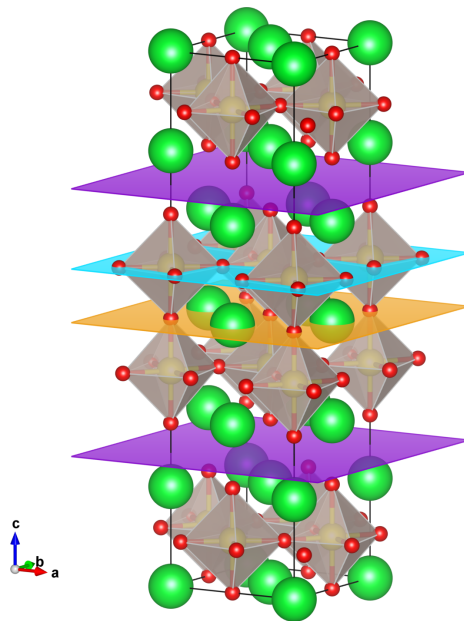


Figure 1: Orthorhombic $Bbcb$ $Sr_3Ru_2O_7$ crystal structure with the calculated cleavage planes. The rock-salt like (violet) and SrO (orange) cutting planes are both SrO terminated, while the turquoise cleavage plane is RuO_2 terminated. Sr: green, Ru: yellow, O: red.

an orthorhombic unit cell (space group $Bbcb$) with a square basal plane for $\text{Sr}_3\text{Ru}_2\text{O}_7$ which is referred to as $c(2\times 2)$ structure in the present paper.

The optimized lattice constant of the orthorhombic bulk $\text{Sr}_3\text{Ru}_2\text{O}_7$ unit cell ($a = b = 3.899 \text{ \AA}$, $c = 20.722 \text{ \AA}$) was determined using the van-der-Waals (vdW) corrected optB86b functional. The calculated geometries are in very good agreement with experimental values [14] ($a = b = 3.890 \text{ \AA}$, $c = 20.725 \text{ \AA}$), showing deviations below 0.25%. Compared to experiment, the rotation of the octahedra is slightly larger, a consequence of the increased Ru–O bond lengths. The preferred cleaving plane is between two SrO layers at the rock-salt like interface with a calculated surface energy of 49 meV/\AA^2 , consistent with previous experiments [8].

We have also calculated the surface energies of the (001) cleaving planes at the SrO and the RuO_2 interface, which yield surface energies of 76 meV and 114 meV , respectively. In both cases, the strong Ru–O bonds have to be broken, leading to these high values compared to the rock-salt like interface. It can be expected that other planes cutting through Ru–O bonds, like e.g. (100), would be similarly unfavorable.

At the surface, the rotation of the octahedra is slightly increased to 11° . The Ca-doped surface was simulated by replacing a single surface Sr atom of a $c(4\times 4)$ unit cell by a Ca atom, yielding a dopant concentration of 6.25%. The relaxation of the doped structure shows that the Ca dopant occupies the same high symmetry position of the original Sr atom, but is slightly pushed (0.17 \AA) into the surface. The Ca dopant does not significantly change the DOS of the substrate (not shown), since the main difference to the Sr states is found in the position of the Ca $3s$ and $3p$ states at $\approx -20 \text{ eV}$ while the depleted Ca $4s$ states at the Fermi level are rather similar to the Sr $5s$. Close to the Fermi edge, the substrate DOS is dominated by the Ru d and O p states, which play the primary role in the hybridization with the adsorbate. A Scanning Tunneling Microscopy (STM) image simulation of the pristine surface (Fig. 2) exhibits a perfectly regular grid of bright dots at the position of the surface Sr atoms at both positive and negative bias voltages. The Ca-doped surface on the other hand shows the Ca dopant as a dark feature in the bright Sr rows, well in line with experimental measurements [8].

3.2. Low Coverage of O_2^-

In the low coverage case, a single O_2 molecule was adsorbed in the $c(4\times 4)$ model cell, yielding 1/16 monolayer (ML) coverage with respect to the number of surface RuO_6 octahedra. It adsorbs as a charged superoxo O_2^- , indicated by an 12% elongation of the O–O bond to 1.35 \AA . In the optimized geometry, the molecule is tilted by 28.8° and located at a Sr–Sr bridge site, close to one of the neighboring Sr atoms (Figs. 3(a,b)). Both distances $d(\text{O}_1\text{--Sr}_1)$ and $d(\text{O}_2\text{--Sr}_2)$ to the respective closest Sr atom is 2.51 \AA . The octahedra at each side of the adsorbed molecule are tilted away 3° from the $[001]$ axis. The vdW corrected optB86b functional clearly prefers a molecular adsorption ($E_{\text{ads}} = -1.42 \text{ eV}$) compared to the dissociated molecule ($E_{\text{ads}} = -0.67 \text{ eV}$).

On the Ca-doped surface the rotation of the octahedra in the first subsurface layer gives rise to two distinct adsorption configurations close to the Ca dopant. The rotation of the octahedra in the subsurface enables the Ca atom to move more easily in the direction where the octahedra are rotated away from it, giving rise to a “wide” (see Fig. 3(c)) and a “narrow” configuration with respect to the orientation of the adsorbed molecule. In both cases, the O_2^- molecule lies fairly flat (4.7° and 7.9° , respectively) and the adsorption energies are very similar (-1.43 eV and -1.41 eV , respectively). Compared to

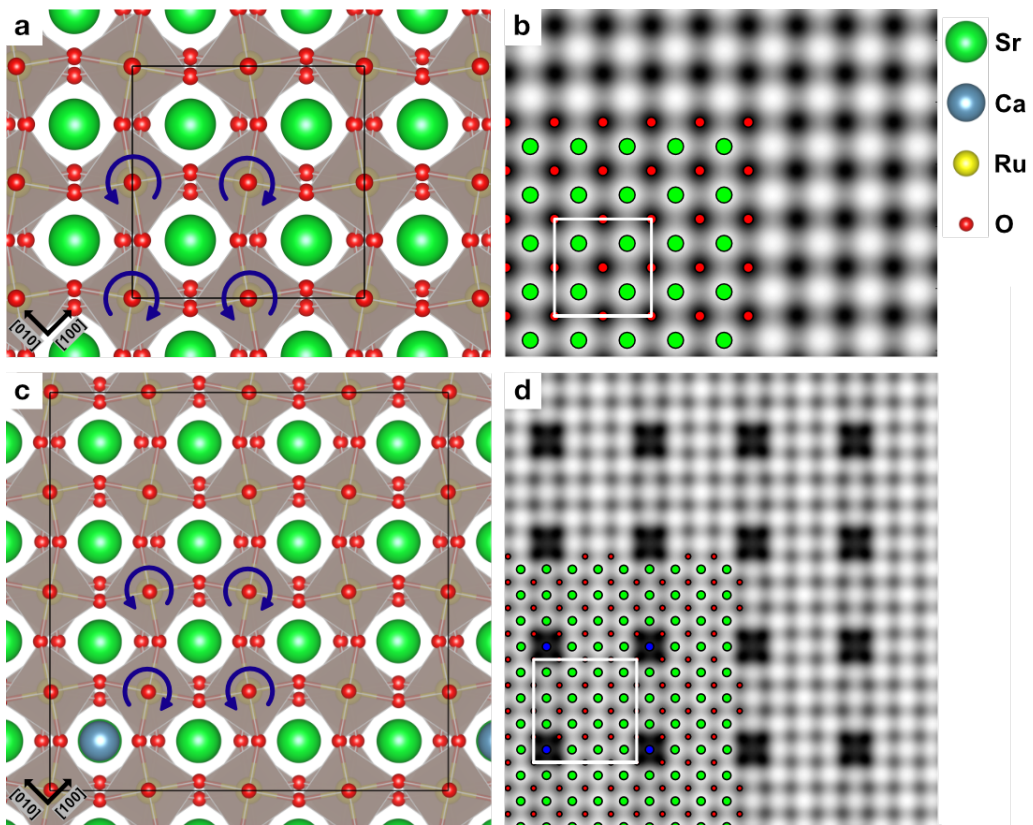


Figure 2: (a): $c(2 \times 2)$ $\text{Sr}_3\text{Ru}_2\text{O}_7(001)$ surface model cell. (b): corresponding STM simulation ($\text{Sr}_3\text{Ru}_2\text{O}_7(001)$), +0.5 V bias voltage. (c): $c(4 \times 4)$ Ca-doped $\text{Sr}_3\text{Ru}_2\text{O}_7(001)$ model cell (6.25% dopant concentration). (d): corresponding STM simulation (Ca-doped $\text{Sr}_3\text{Ru}_2\text{O}_7(001)$), +0.5 V bias voltage.

the undoped case, the atomic distances $d(\text{O}_1\text{-Ca}_1)$ and $d(\text{O}_2\text{-Sr}_2)$ to the closest surface ions change from 2.51 Å to 2.38 Å and 2.60 Å. The Ca dopant is slightly displaced only in the “narrow” adsorption configuration. Interestingly, the most reactive adsorption site was found at a Sr–Sr bridge next to the dopant site (Fig. 3(d), $E_{\text{ads}} = -1.49$ eV), most probably due to the resulting higher flexibility of the surface compared to the undoped case. Inspecting the DOS of an O_2 adsorbed at an Ca–Sr or Sr–Sr bridge site, one finds that the O_2 states shift upwards by about 0.3 eV at Ca–Sr bridges compared to the Sr–Sr bridges, which explains the slightly preferred adsorption at the latter site. Nevertheless, the specific site does not influence the charge state of the adsorbed molecule.

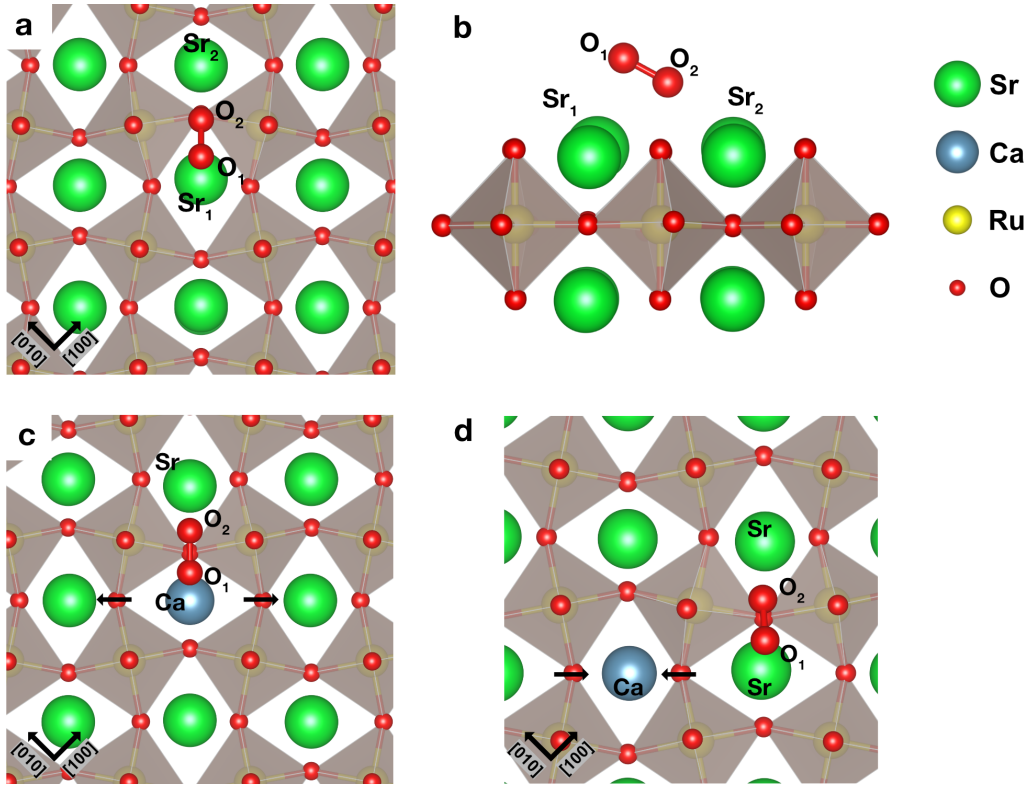


Figure 3: Low coverage of O_2 adsorbed on (a)-(b) pure and (c)-(d) Ca-doped $\text{Sr}_3\text{Ru}_2\text{O}_7(001)$. For Ca-doping, (c) shows the “wide” and (d) the most favored configuration.

3.3. High coverage, from 1/4 monolayer to full coverage

Higher coverages of O_2 molecules were only studied on the undoped system. At 1/4 monolayer (ML) coverage the O_2 adsorbs at a Sr–Sr bridge in an geometry similar to the low coverage case. Again, the O_2 is slightly displaced towards one of the Sr ions and is tilted upwards. Due to the charge transfer the oxygen bond length is again increased to 1.35 Å and the Sr–O distances are slightly more symmetric compared to the low coverage case at 2.49 Å and 2.52 Å for $d(\text{O}_1\text{-Sr}_1)$ and $d(\text{O}_2\text{-Sr}_2)$, respectively. The adsorption

energy per molecule is only slightly reduced to -1.40 eV (Tab. 1), indicating only a rather small adsorbate-adsorbate interaction for the $1/4$ ML coverage regime.

Two typical simulated STM images are shown in Fig. 4(b) and Fig. 4(c). The adsorbed molecules are imaged as a protrusion centered at the high O-atom of the tilted O_2^- . Upon adsorption, the charge transfer to the O_2^- molecule breaks the 2-fold degeneracy of the triplet $2p-\pi^*$ molecular orbital and splits the orbital into a fully occupied $2p-\pi_\perp^*$ orbital perpendicular to the surface and a half-filled $2p-\pi_\parallel^*$ orbital parallel to the surface [7], where the latter is clearly visible in the simulations at positive bias voltage.

Upon increasing the O_2^- coverage the adsorbed oxygen molecules start to experience repulsive interactions (see Tab. 1). For a coverage of $1/2$ ML (two O_2 molecules in a $c(2\times 2)$ model cell) more complex adsorption configurations start to form. On the DFT level the fully relaxed structures show that neither the formation of parallel O_2^- lines along the $[010]$ direction ($E_{\text{ads}} = -0.98$ eV, see Fig. 4(d)) nor along the $[100]$ direction ($E_{\text{ads}} = -1.00$ eV) is favored, as a zig-zag arrangement of the molecules (Fig. 4(e)) leads to an increased adsorption energy per molecule of $E_{\text{ads}} = -1.12$ eV. In that case, every other bridge site is occupied and the rows are shifted by half a unit cell. Additionally, the potential energy landscape of adsorption is very shallow, allowing a multitude of adsorption configurations: also a rotation of up to 18° away from the Sr–Sr bridge orientation is energetically almost degenerated (≈ 10 meV). This rotation is also coupled with an increase in the tilting angle from around 1° to a value of up to 27° .

Interestingly, the DFT calculations predict a clustering of the O_2^- molecules at a Sr atom in the most stable adsorption configuration with an adsorption energy per O_2^- of $E_{\text{ads}} = -1.14$ eV, shown in Fig. 4(f). In this configuration, both O_2^- molecules are tilted from the surface by 27° and share an angle of 14° between each other.

The full coverage limit, i.e. one O_2^- per RuO_6 octahedron, was investigated with four oxygen molecules in the $c(2\times 2)$ surface unit cell. Again, the repulsion between the O_2^- molecules makes a line-wise arrangement unfavorable (Fig. 4(g)). Instead, a low symmetry adsorption configuration is preferred where the O_2^- molecules show a mixture of strongly and weakly tilted arrangements, grouped around a surface Sr atom. The oxygen molecules are displaced from the Sr–Sr bridge sites to a Sr–O bridge site between a surface ion and the apical O of a nearby RuO_6 octahedron, as shown in Figs. 4(h,i). Two clustered configurations were found: In the most favored case, shown in Fig. 4(i) ($E_{\text{ads}} = -0.95$ eV), the oxygen molecules are clustered in groups of two around an apical oxygen atom, where one oxygen of each molecule is located at the centre of a Sr–Sr bridge, while the other oxygen is tilted upwards by 16° to 30° and rotated towards a Sr–O bridge. The octahedra around which the O_2^- molecules are grouped tilt by 4° and 8° . The two mentioned groups show a mirror symmetry along the $(1\bar{1}0)$ plane, the molecules therefore form a slightly wavy double line along the $[\bar{1}10]$ direction. The O–O length is slightly reduced to 1.28 Å. A similar arrangement, shown in Fig. 4(h), where the two groups are rotated by an angle of 90° towards each other yields an energy penalty of 20 meV. In this arrangement all O_2^- molecules are clustered around a surface Sr and tilt by 21° to 23° .

3.4. RPA adsorption energies

As shown in a recent publication [7], the vdW-DF functional strongly overestimates the adsorption energies of the superoxo species on $\text{Ca}_3\text{Ru}_2\text{O}_7$, in part due to the overestimation of the electron affinity of the O_2 molecule. We therefore evaluated potential

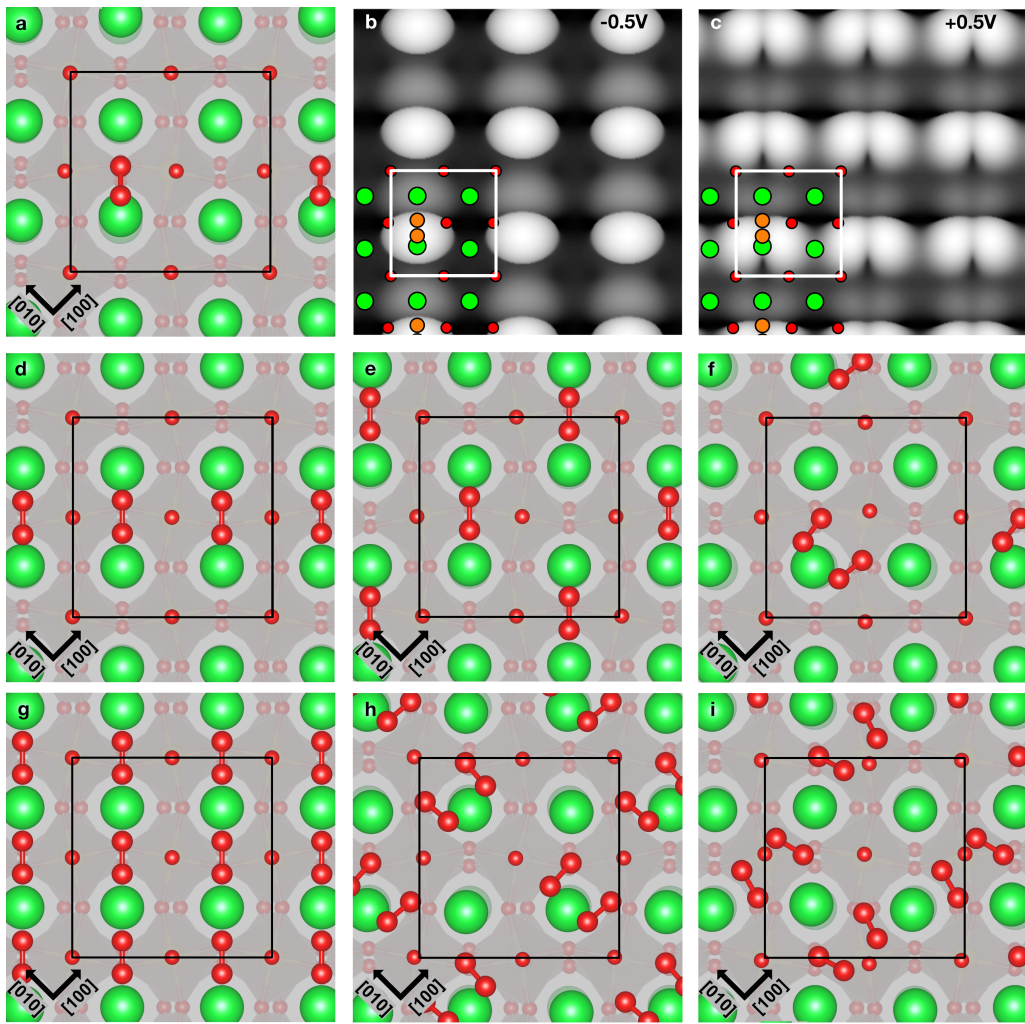


Figure 4: High coverage structures. (a)-(c): 1/4 ML coverage of O_2 located at a Sr-Sr bridge site. STM simulations show (b) a single bright feature at -0.5 V bias voltage and (c) a double lobed bright feature at $+0.5\text{ V}$ bias voltage. The bright blob is separated along the directional axis of the O_2 . (d)-(f): 1/2 ML coverage, O_2 arranged in a parallel, zig-zag and clustered order, respectively. (g)-(i): full coverage structures for the line, rotated clustered, and parallel clustered arrangements, respectively.

Table 1: O₂ adsorption energy per molecule on Ca-doped and pure Sr₃Ru₂O₇(001).

	E_{ads} [eV/O ₂]		
	optB86b	HSE06	RPA
1/16 ML coverage			
Sr-Sr	-1.42		
Sr-Sr, near Ca	-1.49		
Ca-Sr, wide	-1.43		
Ca-Sr, narrow	-1.41		
1/4 ML coverage			
Tilted	-1.40	-0.91	-0.99
Dissociated	-0.67	-0.09	-0.02
1/2 ML coverage			
Parallel	-0.98	-0.68	-0.82
Zig-zag	-1.11	-0.75	-0.85
Clustered	-1.14	-0.29	-0.52
full 1 ML coverage			
Sr-Sr bridge, line	-0.82	-0.43	-0.49
Clustered, parallel	-0.95	-0.07	-0.33
Clustered, rotated	-0.92	-0.01	-0.25

error bars by performing many-electron (RPA) total energy calculations for both the low and high coverage limit structures (1/4 ML and full coverage, respectively) in the small $c(2 \times 2)$ unit cell. Already in the low-coverage case of 1/4 ML our results show that the adsorption energy per O₂ is reduced by ~ 0.4 eV on the RPA level (Tab. 1), nearly identical to the value found for Ca₃Ru₂O₇. Additionally, the RPA values for the coverage of 1/2 ML indicate that the repulsion between the O₂ molecules is underestimated on the DFT level. While the adsorption energy per O₂ of the regular (parallel or zig-zag) structures is again reduced by ~ 0.2 - 0.3 eV (Tab. 1), the most stable DFT configuration where the O₂ are clustered at a surface cation is now strongly disfavored ($E_{\text{ads}} = -0.52$ eV). In addition to the much smaller geometric distance between the O₂ molecules, an additional contribution to the enhanced repulsion can tentatively be assigned to the different hybridization of the clustered O₂ molecules with the surface. In contrast to the regular (line-wise) adsorption configurations, where the additional electron is transferred to the originally unoccupied O₂ $2p-\pi_{\parallel}^*$ orbital (see discussion below), the additional tilting of the O₂ molecule in the cluster configuration results in a rehybridization where the O₂ $2p-\pi_{\perp}^*$ orbital is also partially emptied. This fractional occupation is already strongly penalized on the HSE level, and a similar effect is observed on the RPA level (see Tab. 1).

This trend continues at full coverage. In contrast to the DFT results, where the adsorption energy per O₂ of the favored cluster configuration is just about 0.19 eV lower compared to the most favored 1/2 ML coverage structure, the RPA results show enhanced repulsion for this configuration. Consequently, on the RPA level the most stable configuration is the double line structure with an adsorption energy of 0.49 meV per O₂.

The rather large differences between the DFT (optB86b) and RPA results are also clearly reflected in a predicted phase diagram for O_2 adsorption (see Fig. 5). The DFT results suggest that a full monolayer can be reached under typical ultra-high vacuum conditions of 10^{-11} mbar and liquid nitrogen temperatures, which corresponds to an oxygen chemical potential of $\mu_O = -0.15$ eV. DFT also shows clustered and line configurations to be equally stable. However, the phase diagram based on the RPA values makes a full monolayer unlikely and clearly favors evenly spaced adsorbate configurations.

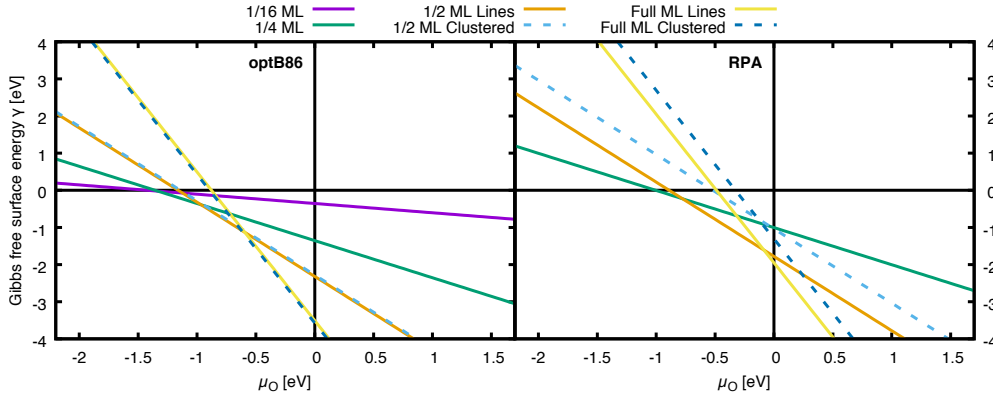


Figure 5: Phase diagrams of adsorption calculated with the optB86b vdW-DFT functional and the many-electron RPA method as a function of the chemical potential μ_O of oxygen. The correspondence between the labelled lines and the adsorption configurations is as follows: 1/16 ML \rightarrow Fig. 3(a), 1/4 ML \rightarrow Fig. 4(a), 1/2 ML Lines \rightarrow Fig. 4(d), 1/2 ML Clustered \rightarrow Fig. 4(f), Full ML Lines \rightarrow Fig. 4(g), Full ML Clustered \rightarrow Fig. 4(i).

3.5. Oxygen Charge State

The calculated spin-polarized Density-of-States (DOS) of the adsorbed oxygen molecule displayed in Fig. 7 reveals a charge transfer to the adsorbed O_2 , which creates a charged superoxo O_2^- species at all coverages on both bare and Ca-doped $Sr_3Ru_2O_7(001)$. The originally half-filled $O_2-2p-\pi^*$ molecular orbital has its two-fold degeneracy lifted upon adsorption and the charge is transferred to the lower lying empty $O_2-2p-\pi_{\perp}^*$ spin-down channel. Particularly at low coverage, the now fully occupied $O_2-2p-\pi_{\perp}^*$ molecular orbital points towards the surface Sr ions. As shown for the high coverage limit in Fig. 6, the charge originates from the RuO_2 layer of the substrate while the surface Sr atoms close to the adsorption site do not contribute at all, as we have shown for the $O_2/Ca_3Ru_2O_7(001)$ system [15]. The Sr and O ions at the interface close to the adsorbate are just slightly polarized. An analysis of Bader charges [16–18] shows that the Ca and Sr formal charge of +2 is unchanged at all coverages. The evaluation of the vibrational frequencies at 1/4 ML coverage shows a red shift to 1132 cm^{-1} of the stretching mode of the O_2^- , which fits well to the experimental value of a charged O_2^- in the gas phase [19]. The calculations do not yield an unstable mode.

However, a closer inspection of the DOS also reveals the shortcomings of a DFT description of the charged O_2 molecule. As shown in Fig. 7, the HOMO-LUMO gap of

the O_2^- molecule as calculated by DFT is too small (0.5 eV) and as a consequence the electron affinity of an adsorbed O_2 molecule is overestimated, i.e. the cost to transfer charge is decreased. As a result a too large adsorption energy per O_2^- , which is referenced to the neutral O_2 molecule, is predicted. This issue can be alleviated by using a hybrid DFT functional like HSE06 or a post-DFT many-electron ansatz like G_0W_0 . For 1/4 ML coverage, the HOMO-LUMO gap of the O_2^- molecule is increased to 3.1 eV and the predicted adsorption energy per O_2^- is reduced to -0.59 eV. Using the many-electron G_0W_0 approximation the HOMO-LUMO gap is increased to 3.4 eV and the corresponding RPA adsorption energy per O_2^- is -0.99 eV. This trend continues for 1/2 ML coverage, here the HSE06 and G_0W_0 HOMO-LUMO gap of the adsorbed O_2^- is increased to 2.9 eV and 3 eV, respectively. At full coverage for the most stable structure, the double line adsorption configuration depicted in Fig. 4(g), the increase of the HOMO-LUMO gap over the DFT estimate is less pronounced for both HSE06 and G_0W_0 , presumably due to the broadening of the O_2^- states, caused by an increased adsorbate-adsorbate interaction. While the DFT DOS for the higher coverage structures might suggest coexistence of differently charged oxygen molecules, the examination of the DOS of the individual molecules shows that all contain the same amount of charge, identified as superoxo O_2^- .

Further charging of the O_2^- molecule yielding a peroxy species only occurs in the presence of additionally available electrons. In contrast to the adsorption of O_2 on La_2NiO_4 where the electron is supplied by the surface cation [6], the Bader charge density analysis for the present case shows that the formal charge on either Ca or Sr is unchanged from the +2 on the clean surface. However, by artificially charging the unit cell at 1/4 ML coverage a peroxy species is formed at the DFT level of theory with an energy penalty of about 0.4 eV, which roughly corresponds to the energy of the unoccupied $2p-\pi^*$ orbital of the superoxo species with respect to the substrate Fermi level. However, as mentioned before, this penalty is again strongly biased by the too small HOMO-LUMO gap of the O_2^- superoxide. Therefore, at the more appropriate many-electron (G_0W_0) level of theory, which yields a larger HOMO-LUMO gap, the stability of a peroxy species is expected to be much lower.

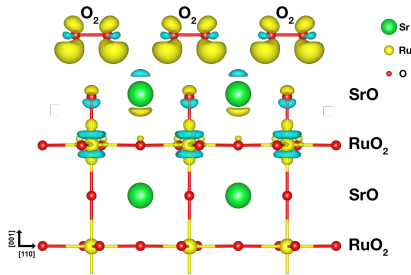


Figure 6: Charge density difference plot at full O_2 coverage calculated with the optB86b functional. Yellow and turquoise areas indicate charged and depleted areas, respectively.

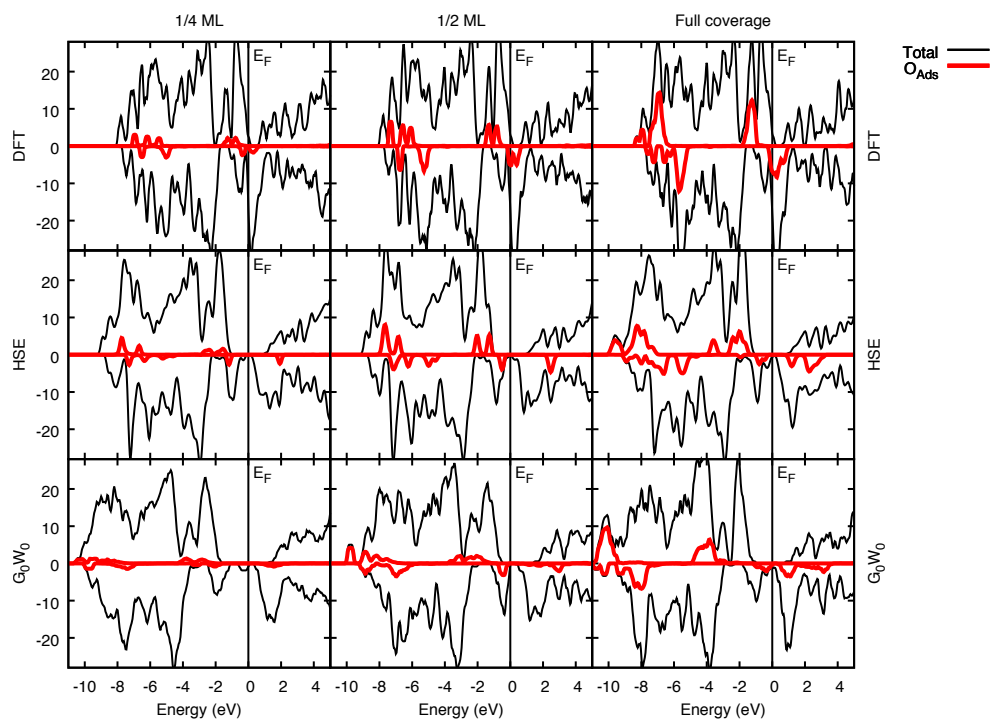


Figure 7: Density of states (DOS) for 1/4 ML, 1/2 ML, and full ML O₂ coverage calculated with the optB86b and HSE06 functional, and the post-DFT many-electron G₀W₀ method.

4. Discussion

According to our recent findings [7], O_2 adsorbs as a superoxo O_2^- species on the $Ca_3Ru_2O_7(001)$ surface at all coverages. Although $Sr_3Ru_2O_7$ is closely related to $Ca_3Ru_2O_7$, there is a structural difference due to the additional tilting of the RuO_6 octahedra in $Ca_3Ru_2O_7$. This tilting causes a channel-like pattern of wider and narrower surface oxygen rows at the CaO terminated $Ca_3Ru_2O_7(001)$ surface, while the symmetry of the SrO terminated $Sr_3Ru_2O_7(001)$ surface layer is identical to square symmetry of a binary rock-salt $SrO(001)$, albeit at an expanded $Sr_3Ru_2O_7$ lattice constant. One way to disentangle the structural effects from the chemical modifications due to the different cation termination is to study Ca -doped $Sr_3Ru_2O_7(001)$. On both surfaces the O_2 molecules preferentially adsorb at or near a cation-cation bridge as a charged superoxo O_2^- molecule.

To accommodate for the optimal atomic distance to the $Sr_3Ru_2O_7$ surface cation, the O_2^- shifts towards one of the surface Sr , and tilts upwards at the same angle, 29° , as on $Ca_3Ru_2O_7(001)$. Inserting a Ca dopant in the $Sr_3Ru_2O_7(001)$ surface layer results in a nearly identical adsorption energy at the Ca - Sr site. Nevertheless, a moderate increase of the adsorption energy by ~ 80 meV is found for the Sr - Sr site next to the Ca dopant. At higher coverages, the structural differences of the adsorption configurations on $Sr_3Ru_2O_7$ and $Ca_3Ru_2O_7$ subside. Like on $Ca_3Ru_2O_7(001)$, at $1/2$ ML coverage the adsorbed O_2^- molecules start to rotate away from the highly symmetric Sr - Sr bridge sites towards the Sr - O bridge positions between a surface ion and the apical oxygen of a nearby octahedron. Our calculations show a slightly higher adsorption energy on $Sr_3Ru_2O_7$ compared to $Ca_3Ru_2O_7$. However, as observed for $Ca_3Ru_2O_7(001)$ [7], the adsorption energy of an O_2 molecule on $Sr_3Ru_2O_7(001)$ is significantly overestimated, partially due to the overestimation of the O_2 electron affinity. A comparison to the values derived from many-electron (RPA) calculations shows a decrease of about 0.4 eV for both $Ca_3Ru_2O_7(001)$ and $Sr_3Ru_2O_7(001)$.

The most striking difference between the adsorption of O_2 on $Sr_3Ru_2O_7$ and $Ca_3Ru_2O_7$ is related to surface structure: While the channel structure of the $Ca_3Ru_2O_7$ surface strongly restricts the accessible surface sites, the high symmetry of the $Sr_3Ru_2O_7$ surface layer leads to flat DFT potential energy surface for the adsorption, and consequently a higher number of energetically nearly degenerated configurations at increased O_2^- coverage. These configurations include O_2^- clusters with a fractional occupation of the O_2 $2p-\pi^*$ orbitals. However, the RPA calculations reveal that the clustered configurations are an artifact of the (vdW) DFT, and yield higher stability for adsorption at Sr - Sr bridges, in line with the findings for O_2^- on $Ca_3Ru_2O_7(001)$. Furthermore the RPA surface O_2 phase diagram clearly predicts that higher O_2^- coverages than $1/2$ ML are quite unlikely on $Sr_3Ru_2O_7(001)$, which is in accord with the findings on $Ca_3Ru_2O_7(001)$ where a saturation coverage of 1 ML was found, corresponding to a $1/2$ ML coverage on $Sr_3Ru_2O_7(001)$.

5. Conclusion

To summarize, the main adsorption mechanism of O_2 on $Sr_3Ru_2O_7(001)$ is very similar to $Ca_3Ru_2O_7(001)$ [7]. This concerns both the preferred adsorption sites at or near Sr - Sr bridges and the charging of the adsorbed O_2^- molecule by a charge transfer from the subsurface RuO_2 layer, without the necessity of dopants or surface defects. The main

difference is related to the higher symmetry of the $\text{Sr}_3\text{Ru}_2\text{O}_7$ surface, which allows for an increased number of adsorption configurations. Yet our results show a pronounced shortcoming in the DFT description of the electronic structure, resulting in an overestimation of the adsorption energies. The comparison with many-electron approaches (G_0W_0 and RPA) suggests an overestimation of the vdW-DF adsorption energies about 0.4 eV, resulting in values of -0.99 eV and -0.49 eV for low and high coverages respectively. Additionally, they strongly disfavor the formation of local O_2^- clusters predicted by standard DFT functionals.

Acknowledgments

This work was supported by the Austrian Science Fund (FWF project F45 “FOXSI”) and the Vienna Scientific Cluster (VSC). The structural models were created with the program VESTA [20].

References

- [1] S. Royer, D. Duprez, S. Kaliaguine, Oxygen mobility in LaCoO_3 perovskites, *Catal. Today* 112 (2006) 99–102.
- [2] J. Suntivich, H. A. Gasteiger, N. Yabuuchi, H. Nakanishi, J. B. Goodenough, Y. Shao-Horn, Design principles for oxygen-reduction activity on perovskite oxide catalysts for fuel cells and metal–air batteries, *Nat. Chem.* 3 (2011) 647–647.
- [3] K. J. May, C. E. Carlton, K. A. Stoerzinger, M. Risch, J. Suntivich, Y. L. Lee, A. Grimaud, Y. Shao-Horn, Influence of oxygen evolution during water oxidation on the surface of perovskite oxide catalysts, *J. Phys. Chem. Lett.* 3 (2012) 3264–3270.
- [4] R. a. Rincón, J. Masa, S. Mehrpour, F. Tietz, W. Schuhmann, Activation of oxygen evolving perovskites for oxygen reduction by functionalization with $\text{Fe-N}_x/\text{C}$ groups, *Chem. Commun.* 50 (2014) 14760–14762.
- [5] A. Staykov, H. Téllez, T. Akbay, J. Druce, T. Ishihara, J. Kilner, Oxygen activation and dissociation on transition metal free perovskite surfaces, *Chem. Mater.* 27 (2015) 8273–8281.
- [6] T. Akbay, A. Staykov, J. Druce, H. Téllez, T. Ishihara, J. A. Kilner, The interaction of molecular oxygen on LaO terminated surfaces of La_2NiO_4 , *J. Mater. Chem. A* 4 (2016) 13113–13124.
- [7] D. Halwidl, W. Mayr-Schmölzer, M. Setvin, D. Fobes, J. Peng, Z. Mao, M. Schmid, F. Mittendorfer, J. Redinger, U. Diebold, A full monolayer of superoxide: oxygen activation on the unmodified $\text{Ca}_3\text{Ru}_2\text{O}_7(001)$ surface, *J. Mater. Chem. A* 6 (2018) 5703–5713.
- [8] B. Stöger, M. Hieckel, F. Mittendorfer, Z. Wang, M. Schmid, G. S. Parkinson, D. Fobes, J. Peng, J. E. Ortmann, A. Limbeck, Z. Mao, J. Redinger, U. Diebold, Point defects at cleaved $\text{Sr}_{n+1}\text{Ru}_n\text{O}_{3n+1}$ surfaces, *Phys. Rev. B* 90 (2014) 165438 (6pp).
- [9] G. Kresse, D. Joubert, From ultrasoft pseudopotentials to the projector augmented-wave method, *Phys. Rev. B* 59 (1999) 1758–1775.
- [10] J. Klimeš, D. R. Bowler, A. Michaelides, Chemical accuracy for the van der Waals density functional, *J. Phys. Condens. Matter* 22 (2010) 022201 (5pp).
- [11] J. Klimeš, D. Bowler, A. Michaelides, Van der Waals density functionals applied to solids, *Phys. Rev. B* 83 (2011) 1–13.
- [12] A. V. Krugau, O. A. Vydrov, A. F. Izmaylov, G. E. Scuseria, Influence of the exchange screening parameter on the performance of screened hybrid functionals, *J. Chem. Phys.* 125 (2006) 224106 (5pp).
- [13] M. Kaltak, J. Klimeš, G. Kresse, Cubic scaling algorithm for the random phase approximation: self-interstitials and vacancies in Si, *Phys. Rev. B* 90 (2014) 054115 (11pp).
- [14] H. Shaked, J. Jorgensen, O. Chmaissem, S. Ikeda, Y. Maeno, Neutron diffraction study of the structural distortions in $\text{Sr}_3\text{Ru}_2\text{O}_7$, *J. Solid State Chem.* 154 (2000) 361–367.
- [15] D. Halwidl, W. Mayr-Schmölzer, D. Fobes, J. Peng, Z. Mao, M. Schmid, F. Mittendorfer, J. Redinger, U. Diebold, Ordered hydroxyls on $\text{Ca}_3\text{Ru}_2\text{O}_7(001)$, *Nat. Commun.* 8 (2017) 23 (8pp).

- [16] G. Henkelman, A. Arnaldsson, H. Jónsson, A fast and robust algorithm for Bader decomposition of charge density, *Comput. Mater. Sci.* 36 (2006) 354–360.
- [17] E. Sanville, S. D. Kenny, R. Smith, G. Henkelman, Improved grid-based algorithm for Bader charge allocation, *J. Comput. Chem.* 28 (2007) 899–908.
- [18] W. Tang, E. Sanville, G. Henkelman, A grid-based Bader analysis algorithm without lattice bias, *J. Phys. Condens. Matter* 21 (2009) 084204 (7pp).
- [19] P. H. Krupenie, The spectrum of molecular oxygen, *J. Phys. Chem. Ref. Data* 1 (2) (1972) 423–534.
- [20] K. Momma, F. Izumi, *VESTA3* for three-dimensional visualization of crystal, volumetric and morphology data, *J. Appl. Cryst.* 44 (2011) 1272–1276.